Structure and Motion of Edge Turbulence in NSTX and Alcator C-Mod

S.J. Zweben, Princeton Plasma Physics Laboratory, Princeton, NJ 08540
R.J. Maqueda, Nova Photonics, Princeton, NJ 08540
J.L. Terry, MIT, Cambridge, Mass. 02139
T. Munsat, Univ. Colorado, Boulder, Co. 80309
J.R. Myra, D. D'Ippolito, D.A. Russell, Lodestar Research, Boulder, Co 80301
J.A. Krommes, B. LeBlanc, T. Stoltzfus-Dueck, D.P Stotler, K.M. Williams, Princeton Plasma Physics Laboratory, Princeton, NJ 08540
C.E. Bush, R. Maingi, ORNL, Oak Ridge, Tenn. 37831
O. Grulke, MPI for Plasma Physics, Euratom Association. Greifswald, Germany
S.A. Sabbagh, Columbia University, NY, NY 10027
A.E. White, UCLA, Los Angeles, Cal. 90095

ABSTRACT

This paper compares the structure and motion of edge turbulence observed in L-mode and H-mode plasmas in the National Spherical Torus Experiment (NSTX) [1]. The radial and poloidal correlation lengths are not significantly different between L-mode and H-mode in the cases examined. The poloidal velocity fluctuations are lower and the radial profiles are somewhat flatter in H-mode compared with L-mode plasmas. These results are compared with similar measurements Alcator C-Mod [2] and with theoretical models.

1. Introduction

Edge turbulence has been measured for many years in tokamaks and other toroidal magnetic fusion devices, most recently using 2-D diagnostic techniques [3-5]. The results have been fairly consistent over a wide variety of devices; namely, that the edge is strongly unstable in the “drift wave” range of size scales (~0.1 to 10 cm) and frequencies (~10 kHz to 1000 kHz), with typical density fluctuation levels $\tilde{n}/n \sim 5\text{-}50\%$ near the last closed magnetic flux surface, at least at the outboard midplane. This edge turbulence is important since it dominates radial transport in the scrape-off layer, which affects the plasma-wall interaction, and since it probably determines the H-mode threshold, which affects the global plasma confinement.

Despite a wealth of experimental data there is so far little direct comparison of these edge turbulence measurements with first-principles turbulence models or simulations. However, these models have been evolving rapidly [6-10], so direct comparisons are becoming more feasible. This paper presents recent edge turbulence imaging data from NSTX and briefly compares the results to Alcator C-Mod and to some recent theoretical models.

Section 2 describes the edge turbulence diagnostic used for these measurements, and Section 3 describes the recent NSTX results. The discussion of Section 4 contains a comparison between NSTX and Alcator C-Mod, a comparison with theoretical models, directions for future work, and a conclusion.

2. Gas Puff Imaging Diagnostic

The gas puff imaging (GPI) diagnostic used for these turbulence imaging measurements has been described extensively in Refs. 11-15. For the present paper the visible D_α (656 nm) line emission from a deuterium gas puff was used to image the turbulent fluctuations. Since the turbulence is highly elongated along the magnetic field

B, the visible light from the gas puff cloud was viewed along the local (total) B field in the cloud (to within a few degrees) to image the radial and poloidal structure of the turbulence. The gas cloud increases the brightness of the emission and localizes it along this viewing line for improved spatial resolution.

Some hardware improvements were made to the GPI diagnostic compared to that described previously. First, an 8x10 mm coherent fiber optic bundle was used instead of a 4x4 mm bundle, which increased the signal level by about a factor of 5. Second, the gas puff manifold was moved closer to the plasma edge to decrease the toroidal extent of the gas cloud so as to improve the spatial resolution, which is now about 1-2 cm. Third, a new Princeton Scientific Instruments PSI-5 camera was used; this camera can store 300 frames with spatial resolution of 64 pixels (poloidally) x 64 pixels (radially), compared with 28 frames for the previous PSI-4 camera [11]. At the normal frame rate of 250,000 frames/sec the PSI-5 camera captures 1.2 msec of data for each NSTX shot.

Figure 1(a) shows a typical image of a single frame from the PSI-5 camera. The field of view at the plasma is 23 cm radially by 23 cm poloidally centered near the magnetic separatrix about 20 cm above the outer midplane of NSTX (R=85 cm, a=65 cm). The orientation of the bundle is arranged so that the local radial direction is horizontal (outward to the right) and the local poloidal direction (within a magnetic flux surface) is vertical, with the ion diamagnetic and grad-B drift direction down. Superimposed on this image are the locations of 13 discrete "chords", the light from each of which was coupled to a photomultiplier tube and digitized at 500 kHz for 64 msec, At the GPI gas cloud the chord centers were separated by 2 cm and viewed a diameter of 2 cm. A typical signal vs. time from one of these chords is shown in Fig. 1(b). The analog bandwidth of these chord signals was ≈ 200 kHz.

The interpretation of the GPI images has already been described [11-15]. The light emission in the D_α line is located in the region where the neutrals are significantly excited but not yet ionized, which corresponds roughly to $T_e \approx 5\text{-}100$ eV. Within this temperature range, which is roughly ±5 cm around the separatrix in NSTX, the line emission at a given neutral density is a nonlinear (but monotonically increasing) function of the local electron density n_e and electron temperature T_e [15]. However. as discussed in Ref. 11, the structure and motion of the GPI light fluctuations, as defined by the space-time cross-correlation functions, is approximately independent of the details of this nonlinearity. This effect is similar to a TV image in which the structure and motion is independent of the nonlinearity controlled by the contrast setting. For the camera images in this paper there was an addition nonlinearity due to the micro channel plate of the PSI-5 camera, for which the output signal level was roughly proportional to the square root of the light intensity over this range of intensities. This nonlinearity had no effect on the chord signals.

3. NSTX Results

a) Plasma parameters

Most of the results described in this paper were obtained for a set of about 20 discharges taken on a single run day with plasma parameters shown in Table 1 (#113732-113750). These discharges had a relatively small toroidal field (3 kG) and a modest amount of NBI power (2-4 MW); nevertheless, their qualitative behavior was similar to other NBI-heated L-mode and H-mode discharges in NSTX [11]. All of these discharges had L-mode to H-mode transitions which were captured in either the camera data or the chord data, or both. Shots #113732-45 had an upper-single-null configuration; shots #113747-50 had the same plasma parameters but with a lower-single-null.

Figure 2 shows the edge plasma parameters for the discharges described in this paper, as summarized in Table 1. The radial coordinate is the major radius at the outer midplane. The GPI signal intensity profiles come from the time-averaged camera images as mapped along a flux surface to the outer midplane, and span a radial region about ±5 cm around the magnetic separatrix (as derived from EFIT). The n_e and T_e profiles come from Thomson scattering for four similar shots in this sequence, all taken ±8 msec with respect to the L-H transition. The increase in the edge density and temperature just after the L-H transition can be seen, although the details of the profile shape are difficult to determine, given the relatively coarse space and time resolution of the Thomson scattering system. Note that the GPI light emission during H-mode peaks within the density gradient region of the pedestal.

b) Qualitative Description of the Data

An example of the image data from a shot with an L-H transition is shown in Figure 3 (#113732). This mosaic shows 48 successive frames from a 300 frame movie, each of which was exposed for 4 μsec with the field of view of Fig. 1. The only image analysis was "despeckling" with a 3x3 median filter, and only one common intensity normalization was used for all frames. Frames #130-153 were just before the L-H transition, frames #153-161 were during the transition and frames #162-177 were after the transition.

The qualitative impression from the movie of this data is that before the L-H transition the edge turbulence consisted of random-looking fluctuations which moved mostly downward, but sometimes upward, with occasional isolated "blobs" forming in the brightest regions and moving radially outward. After the transition, the visible region narrowed and became much more quiescent, with the fluctuations moving more uniformly downward, and with less frequent blob generation. During the transition the structures and motions seem to "morph" smoothly between these two conditions without the appearance of any new structure or motion. It looks as if the turbulence was "turned off" somewhere else, since there was no obvious "trigger" for the L-to-H-mode transition within this field of view. On the other hand, the few available images of H-mode to L-mode transitions do seem to show a local small-scale instability growing into blob-like radial motion within the GPI view [16].

Obviously such qualitative impressions are subjective and not conclusive. However, it has been quite difficult to formulate analysis tools which could quantify these impressions, perhaps because our brains are so good at pattern recognition and tracking. The following sections describe the quantitative analysis done so far.

c) Structure Analysis

We define the cross-correlation function between two time series signals "S_o" and "$S_{\Delta x}$" which are separated by a distance "Δx" (radially or poloidally), and by an artificially introduced time delay "Δt", as:

$$C(\Delta x, \Delta t) = \Sigma_t \, S_o(t) \, S_{\Delta x}(t+\Delta t) \qquad [1]$$

where the sum is taken over the common time interval of both signals. The time-averaged value of both signals is removed before this calculation; thus this estimate is not affected by the spatial calibration, and just evaluates the degree of correlation between the temporal behavior at the two points. This cross-correlation function averages over the whole frequency spectrum.

For an estimate of the poloidal correlation length the time delay was set to $\Delta t=0$ and the value of C between the central chord and the other chords in the poloidal array (each separated by $\Delta x=2$ cm) was plotted as a function of their separation. The poloidal correlation length L_{pol} was defined as the full-width at half-maximum (FWHM) of this curve of C vs. Δx (this FWHM is equivalent to ≈1.6 times the half width of a Gaussian of the same shape).

Figure 4(a) shows the time evolution of the poloidal correlation length before and after the L-H transition, as evaluated from the chord arrays for a set of 13 consecutive shots such as described in Sec. 3(a). The horizontal axis is the time of the main (i.e. first) L-H transition, which varies from 0.183-0.202 sec for these shots. Each point represents the correlation length estimated for a 1 msec time interval for that shot (i.e. 500 time points). The central chord in the array was located near the radial peak of the signal, as shown in Figs. 1 and 2. The result was that the poloidal correlation had an average value of L_{pol}≈6.3±1.2 cm before the transition, 7.5±2 cm after the transition, and 6.8±1.5 cm overall. There appeared to be a slow increase in L_{pol} over time ±20 msec around the transition, but there was little if any change in L_{pol} within ±1 msec of the transition. The second-to-innermost channel was not working properly for this data so a linear interpolation was used instead of it. Correlation lengths below 2 cm were not accessible due to the finite spacing of these chords.

For the radial correlation length estimate in Fig. 4(b) the FWHM was determined by correlating the central radial chord with the two radial chords ±4 cm inside and outside of it (the two radial chords adjacent to the central chord were not working properly for these shots). The FWHM of this 3-point cross-correlation function (linearly interpolated) is plotted in Fig. 4(b), with the result that L_{rad}≈ 4.3±0.8 before the L-H transition, 5.2±1.2 after the transition, and 4.8±1 cm overall. Since the spacing of these chords is comparable to the radial correlation length, some of these data points probably belong inside the "inaccessible region" below L_{rad}~4 cm, so these average radial correlation lengths are somewhat overestimated.

The structure of the turbulence was also obtained from the 2-D images in essentially the same way ($\Delta t=0$), although this data existed for only 1.2 msec per shot (i.e. 300 frames at 250,000 frames/sec). In these analyses the poloidal cross-correlation functions were centered at the up/down center of the images, the radial cross-correlation functions were centered at the peak of the time-averaged emission profile to maximize the signal/noise ratio. The correlation analyses were done for each line or column within the range ±2 cm radially and ±5 cm poloidally around these centers. Note that for the H-mode cases this analysis was done in the high gradient region of the edge pedestal, as shown in Fig. 2. The raw data was smoothed by a median filter over 3x3 pixels before analysis.

Figure 5 shows the relationship between L_{pol} and L_{rad} derived this way for 18 shots with the parameters in Table 1. Each of the eleven L-mode points represents one shot of those used in Fig. 4, while the four H-mode points comes from other shots from the same day. The error bars on each point represent the standard deviation with the spatial range of analysis for that shot. The average correlation lengths are similar to those shown in Fig. 5; namely, $L_{pol} \approx 6.3 \pm 1.3$ cm and $L_{rad} \approx 4.2 \pm 0.4$ cm for L-mode, and $L_{pol} \approx 8.9 \pm 1.6$ cm and $L_{rad} \approx 5.3 \pm 1.0$ cm for H-mode, where these error bars represent the shot-to-shot variations. The triangles show two shots in which the L-to-H transition was captured by the camera and the L-mode and H-mode periods of each were analyzed separately (#113732 and #113631). The results are similar to the other points, but perhaps there was a slight reduction in the radial correlation length just after the H-mode transition in these cases.

In summary, the result from Figs. 4 and 5 show no statistically significant change in either the poloidal or radial correlation lengths between the L-mode and H-mode in this data set. Some uncertainties and limitations of these results are discussed in Sec. 4(c).

d) Poloidal Velocity Analysis

Figure 6 shows the poloidal turbulence velocity obtained from the poloidal array of chords, as determined by the time delay of the peak of the cross-correlation functions between the central chord and all other poloidal chords (see Eq. 1). The poloidal velocity was derived from a linear fit to these time delays, and the error bars are the standard deviations of this fit. The same set of 13 consecutive shots of Fig. 4 along with the same 1 msec time bins were used for this analysis. The central chord was located at the time-averaged peak of the signals, which was near or slightly outside the separatrix. The second-to-innermost channel was not working properly for this data so a linear interpolation was used there.

The result of Fig. 6 is that the magnitude of the poloidal velocity at this radius increased from $V_{pol} = -2.9 \pm 1.6$ km/sec in L-mode to -4.3 ± 1.2 km/sec in H-mode (the ion diamagnetic drift velocity direction is negative in this graph). In L-mode most of the variation was due to random scatter, whereas in H-mode the random scatter was considerably reduced and the main variation was a slow time evolution over ~10 msec. Thus the poloidal motion appeared to be more "frozen" in H-mode than in L-mode.

Figure 7 shows the radial profiles of the poloidal turbulence velocity derived from images for four of the L-mode and four of the H-mode shots used in Fig. 5. Each point represents the poloidal velocity derived for one column of the image data for one shot, averaged over the time duration of the image. The radial coordinate is the distance from the separatrix for each shot, and all velocities are in the ion diamagnetic drift direction. The method for determining the velocity was the same as for Fig. 5, except that only points with $C(\Delta x, 0) \geq 0.5$ from the central (up/down centered) pixel in the image were used in the fitting process. One of the H-mode shots in Fig. 7 (with circled points, #113745) was similar to those used in Fig. 6 and showed a similar velocity at that radius (~ 5 km/sec). The other three H-mode cases of Fig. 7 had a lower-single-null instead of an upper-single-null as for the other shots, but still with the parameters shown in Table 1.

The general trend shown in Fig. 7 is for a lower velocity gradient in the H-mode cases compared to L-mode cases within this range of radii. For radial positions $(\tilde{r}\square_{\square\square\square}) \sim 0$ to 5 cm, the average radial gradient in L-mode was roughly $\nabla V_{pol} \sim 1$ (km/sec)/cm $\approx 10^5$ sec^{-1}, while the average gradient in H-mode was roughly $\nabla V_{pol} \sim 0.5$ (km/sec)/cm $\approx 5\text{x}10^4$ sec^{-1}. Obviously there are considerable variations about these averages; on the other hand, at some radii in H-mode the velocity gradient is considerably less than this average. Inside the separatrix the error bars are too large to estimate a gradient for the L-mode cases; however, for at least two of the H-mode cases the gradients inside the separatrix are similar to those outside the separatrix.

The error bars derived from the velocity fits for Fig. 7 were significantly smaller in H-mode than in L-mode shots, similar to the trend seen in Fig. 6. In other words, the fluctuations in the poloidal velocity were lower in H-mode than in L-mode, at least averaged over the 1.2 msec of these images. For example, in the region $\tilde{r}\square_{\square\square\square} > 0$ the error bars for the H-mode cases was typically ±0.15 km/sec, while for the L-mode cases it was typically ±0.3 km/sec.

In summary, the results from Figs. 6 and 7 indicate that the time variations in the poloidal turbulence velocity were lower in H-mode than in L-mode, and the average radial gradient of V_{pol} was somewhat smaller in H-mode than L-mode plasmas, at least outside the separatrix. Some uncertainties and limitations of these results, as discussed below.

e) Limitations and Uncertainties

There are several limitations to the present results: (1) the radial range was limited to about ±5 cm around the separatrix and the poloidal range to ±10 cm just above the outer midplane; (2) the data set was limited to a relatively few (~20) shots at one specific condition, although similar behavior has been seen in a wider range of NSTX discharges [11]; (3) the L-H transition itself was captured by the imaging system in only a very few (~5) shots, due to the limited frame capacity of the present camera; and (4) the velocity profiles were mainly obtained outside the separatrix.

The analysis presented here was limited to the 2-point correlation function, which characterized only the average size and velocity of the turbulence. No attempt was made to determine the 2-D shape or direction of the turbulence, or to evaluate the non-Gaussian or intermittent structure and/or motion.

The main source of uncertainty was the relatively small signal/noise level during H-mode discharges, in which the relative fluctuation level and usable radial range of the GPI signals decreased with respect to L-mode. This may have resulted in a small underestimate of the radial correlation length derived from H-mode images in Fig. 5. On the other hand, the relatively coarse spacing of the available radial chords may have led to a small overestimate of the radial correlation length in Fig. 4. The similarity of these two results suggests that these errors are relatively small.

An additional source of uncertainty was the occasional presence of coherent or quasi-coherent MHD fluctuations in the GPI data. This tends to increase the correlation lengths, since MHD-type fluctuations are globally correlated, and may introduce a component of the fluctuation velocity which is not characteristic of the edge turbulence. However, in the present data set the MHD-type fluctuations were generally quite small.

Finally, the location of the separatrix is uncertain to perhaps ±1-2 cm, even though it was derived using the best available EFIT analysis (in the absence of MSE data). In particular, the temperature at the EFIT separatrix of $T_e \approx$ 10-30 eV (Fig. 2) appears to be too low to account for the power flow across the separatrix, according to the standard edge heat flux model. This may be due to either inaccuracies in EFIT or limitations of the standard model (e.g. non-Maxwellian distribution functions).

4. Discussion

a) Comparison with Alcator C-Mod

A comparison of the main results for L-mode plasmas in NSTX with those derived from a similar GPI diagnostic on Alcator C-Mod is shown in Table 2. The toroidal field and plasma density at the edge are nearly 10 times higher on C-Mod than in NSTX, but the edge electron temperatures in C-Mod are only slightly higher than in NSTX. The radial and poloidal correlation lengths in C-Mod are about 5-10 times shorter than in NSTX, and the poloidal velocity is about 5 times lower in C-Mod than in NSTX. However, the radial velocity in both machines is surprisingly similar, where the radial speeds for NSTX are taken from Ref. 11. Note that most of the GPI data from C-Mod comes from outside the separatrix, since the neutral gas does not penetrate as far in C-mod as it does in NSTX.

b) Connections with Theoretical Models

The usual fluid models for edge turbulence [6-10] predict a broad k-spectrum with an average spatial scale roughly $k_{\perp}\rho_{\square}\,\square\tilde{}\,\square$. The radial correlation lengths in NSTX of L_{rad}(FWHM) ≈ 4 cm agree with this scaling to within about a factor of 2, depending on the radial location. Thus the decrease in turbulence size scale from NSTX to C-Mod is most likely due to the higher toroidal field in C-Mod.

The similarity of the radial turbulence velocity between NSTX and C-Mod can be explained by the "blob model" of edge turbulence propagation (see Ref. 17 and references therein). In this model the speed of isolated structures in the scrape-off layer is determined largely by the electron temperature and major radius, which are similar for both machines. Details of the application of this model to the NSTX data will be described elsewhere [18].

In apparent contrast to the standard ExB flow shear model of the H-mode, the radial correlation lengths were not significantly lower in H-mode than in L-mode (Figs. 4 and 5), and the average poloidal velocity gradient did not appear to be larger in H-mode than in L-mode in the cases examined (Fig. 7). The clearest change seen from L-mode to H-mode was a reduction in the random scatter of the measured poloidal velocity, i.e. the poloidal motion seemed more "frozen" in H-mode than in L-mode. The lack of a clear correlation between velocity shear and the H-mode has been seen previously [19].

However, there are several caveats to keep in mind concerning the interpretation of these results: (1) whatever is causing the H-mode may be outside the field of view of this diagnostic; (2) the poloidal turbulence velocities were averaged over ≈1 msec, so would not have detected any shorter-timescale zonal flows or GAMs; (3) the ExB flow speed itself was not directly measured, only the sum of the ExB drift velocity and the intrinsic phase velocity of the fluctuations, and (4) there are no theoretical simulations of the L-H transition for NSTX, so these results cannot yet be compared to any specific model. Yet it is interesting to note that the estimated shearing rate of this turbulence during H-mode of $\tau_s \sim \nabla V_{pol}\,(L_{rad}/L_{pol}) \sim 2\text{-}3\text{x}10^{4}\ \text{sec}^{-1}$ is similar to the inverse of the measured autocorrelation time $\tau_a \approx 2x10^{-5}$ sec, i.e. near the standard ExB flow-shear-stabilization criterion.

c) Directions for future work

There are many possible directions for further work in this area. The quality of the data could be improved with higher space and time resolution, and the quantity of the data can be greatly improved with a continuous high-frame-rate camera. The analysis of the data could be significantly improved by using higher-order statistical measures, such as the bicoherence spectrum [20], or by developing algorithms to measure the 2-D velocity fields [21]. Ultimately the most important goal is to quantitatively compare the measurements of turbulence with specific theoretical models. Some promising results in this direction have been obtained [22-24], but much remains to be done.

d) Conclusions

This paper compared the structure and motion of edge turbulence observed near the outer midplane magnetic separatrix in L-mode and H-mode plasmas in NSTX. The radial and poloidal correlation lengths were not significantly different between L-mode and H-mode in the cases examined. The time variations in the poloidal velocity were lower in H-mode than in L-mode, and the average radial gradient of V_{pol} was smaller in H-mode than L-mode plasmas, at least outside the separatrix. These results appear to disagree with the standard ExB flow shear-driven model for L-mode to H-mode transitions, but no direct comparison with any theoretical simulation based on this model was made.

Acknowledgments; We thank the NSTX and Alcator C-Mod teams for their support for these experiments, and O.E. Garcia, T.S. Hahm, K. Hallatschek, B.N. Rogers, B.D. Scott, P.W. Terry, M.V. Umansky, and X.Q. Xu for discussions of turbulence simulation and theory. This work was supported by USDOE Contract DE-AC02-76CHO3073 (PPPL) and USDOE Cooperative Agreement DE-FC02-99ER54512 (MIT).

References:

[1] M. Ono, M.G. Bell, R.E. Bell et al, PLASMA PHYSICS AND CONTROLLED FUSION 45: A335-A350 Suppl. 12A, DEC 2003

[2] E.. Marmar, B. Bai, R.L. Boivin et al, NUCLEAR FUSION 43 (12): 1610-1618 DEC 2003

[3] J. Bleuel, M. Endler, H. Niedermeyer et al, New J. Physics 4, 38.1 (2002)

[4] G.R. McKee, R.J. Fonck, M. Jakubowski et al, Phys. Plasmas 10, 1712 (2003)

[5] A. Fredriksen , C. Riccardi, L. Cartegni et al, PLASMA PHYSICS AND CONTROLLED FUSION 45 (5): 721-733 MAY 2003

[6] B.D. Scott, PHYSICS OF PLASMAS 12 (6): Art. No. 062314 JUN 2005

[7] M.V. Umansky, T.D. Rognlien, X.Q. Xu, JOURNAL OF NUCLEAR MATERIALS 337 (1-3): 266-270 MAR 1 2005

[8] O. E. Garcia, N. H. Bian, V. Naulin et al, Phys. Plasmas 12, 090701 (2005)

[9] R. Singh, V. Tangri, P. Kaw, and P. N. Guzdar, Phys. Plasmas 12, 092307 (2005)

[10] P. Beyer P, S. Benkadda, G. Fuhr-Chaudier G et al, PHYSICAL REVIEW LETTERS 94 (10): Art. No. 105001 MAR 18 2005

[11] S.J. Zweben, R.J. Maqueda, D.P. Stotler et al, Nucl. Fus. 44,1 34 (2004)

[12] R.J. Maqueda et al, Rev. Sci. Inst., 2020, 2003

[13] J.L. Terry et al, Phys. Plasmas, 1739, 2003

[14] O. Grulke, J.L. Terry, B. LaBombard, and S.J. Zweben, sub. to Phys. Plasma (2005)

[15] D.P. Stotler, D.A. D'Ippolito, B. LeBlanc B et al.CONTRIBUTIONS TO PLASMA

PHYSICS 44 (1-3): 294-300 2004

[16] S.J. Zweben, C.E. Bush, R.J. Maqueda et al, IEEE Transactions on Plasma Science 33, 446 (2005)

[17] D.A. Russell, D.A. D'Ippolito, J.R. Myra et al.PHYSICAL REVIEW LETTERS 93 (26): Art. No. 265001 DEC 31 2004

[18] J.R. Myra et al, Bull. Am. Phys. Soc. Vol. 50, No. 8, paper RP1 19 (2005)

[19] G.R. Tynan, L. Schmitz, L. Blush et al, Phys. Plasmas 1, 3301 (1994)

[20] G.R. Tynan, R.A. Moyer, M.J. Burin et al. PHYSICS OF PLASMAS 8 (6): 2691-2699 JUN 2001

[21] G. McKee, R.J. Fonck, D.K. Gupta, et al, Rev. Sci. Inst. 75, 3940 (2004)

[22] U. Stroth, F. Greiner, C. Lechte et al, PHYSICS OF PLASMAS 11 (5): 2558-2564 MAY 2004

[23] E. Sanchez, C. Hidalgo C, B. Goncalves et al, .JOURNAL OF NUCLEAR MATERIALS 337 (1-3): 296-300 MAR 1 2005

[24] S. H. Müller, A. Fasoli, B. Labit et al, Phys. Plasmas 12, 090907 (2005)

Table 1: NSTX parameters

R = 0.85 m

a = 0.68 m

B_o = 3 kG

I_p = 0.8 MA

P_{NBI} = 2-4 MW

$T_e(0)$ = 0.5-1 keV

$n_e(0) = 2\text{-}4 \times 10^{13}$ cm^{-3}

$\tau_E \approx$ 30 msec

$\beta_{tor} \approx$ 10%

$n_e(\text{edge}) \approx 0.2\text{-}2 \times 10^{13}$ cm^{-3}

$T_e(\text{edge})$ = 5-50 eV

$L_\perp \sim$ 2-5 cm

$L_{II} \sim$ 5 m

$\rho_s \sim$ 0.2 cm

$\beta_e \sim 10^{-3}$

Table 2: Comparison of NSTX and Alcator C-Mod

	NSTX	Alcator C-Mod*
B_{edge}	2-3 kG	40 kG
n_{edge}	0.2-2	2-20 x 10^{19} cm^{-3}
$T_{e,edge}$	5-50 eV	20-80 eV
L_{pol}	5-9 cm	0.6-1.0 cm
L_{rad}	2-6 cm	0.7-1.5 cm
V_{pol}	$\leq$ 5 km/sec	$\leq$ 1 km/sec
V_{rad}	$\leq$ 1-2 km/sec	$\leq$ 1.5 km/sec

Figure Captions:

1) A single frame from a sequence of 300 images captured by the fast camera during an NSTX discharge. The 64x64 pixel frame shows the GPI light emission in D_α for a region 23 cm poloidally (up/down) by 23 cm radially (left/right) located 20 cm above the outer midplane, with an exposure time of 4 μs. The locations of the radial and poloidal chord arrays are superimposed on the image, along with the locations of the magnetic separatrix and outer limiter shadow. The typical time dependence of the GPI light emission as measured at the central chord is shown in part (b).

2) Radial profiles of the GPI light emission and Thomson scattering measurements for the edge plasmas used for this paper. The GPI signal profiles are the time-averages over the L-mode and H-mode periods as measured by the camera. The locations of the central, innermost, and outermost radial chords is shown at the top. The GPI light emission region has a radial width of $\approx \pm 10$ cm around the magnetic separatrix (as inferred from EFIT). The Thomson scattering profiles with L-mode in black and H-mode in red, were taken within ± 8 msec of the L-H transition for four similar shots. The GPI light emission during H-mode peaks within the density gradient region of the pedestal.

3) An example of the image data from a shot with an L-H transition (#113732). This mosaic shows 48 successive frames from a 300 frame movie, each frame of which was exposed for 4 μsec with the same field of view of as shown in Fig. 1(a). Frames #130-152 were just before the L-H transition, frames #153-161 were during the transition and frames #162-177 were after the transition.

4) Time dependence of the (a) poloidal and (b) radial correlation lengths as inferred from the chord data for a set of 13 consecutive discharges (#113732-113744) for times near the L-H transition. Each point represents the analysis of a 1 msec interval for one of these shots. The poloidal correlation length was $L_{pol} \approx 6.3 \pm 1.2$ cm before the transition and $L_{pol} \approx 7.5 \pm 2$ cm after the transition, and the radial correlation length was $L_{rad} \approx$

4.3±0.8 before the transition and L_{rad}≈5.2±1.2 after the transition (all FWHM). Thus there was no statistically significant difference in either L_{pol} or L_{rad} between L-mode and H-mode. The inaccessible regions due to the finite spacing of the chords are shown in gray.

5) Radial vs. poloidal correlation lengths inferred from the camera images for a set of discharges of various types for this data set. For the L-mode and H-mode cases each point represents the analysis of one shot, with the result that for L-mode, $L_{pol} \approx 6.3\pm1.3$ and $L_{rad} \approx 4.2\pm0.4$ cm, while for H-mode $L_{pol} \approx 8.9\pm1.6$ cm and $L_{rad} \approx 5.3\pm1.0$ cm (all FWHM). For the L-H cases each point represents the analysis of the L-mode vs. the H-mode phase of the same shot. The error bars represent the spatial variation over the regions of analysis. There were no statistically significant variations between L-mode and H-mode in this data set.

6) Time dependence of the poloidal turbulence velocity as inferred from the poloidal array of chords for the same set of discharges as in Fig. 4. The error bars represent the standard deviation of the fits to the velocity profiles over 1 msec time intervals for each shot. At this radius there was a reduction in the random time variation in the poloidal velocity just after the H-mode transition.

7) Radial profiles of the poloidal turbulence velocity inferred from the camera images for four L-mode and four H-mode discharges. In the region near or just outside the separatrix the average radial gradient in the poloidal velocity is smaller in H-mode than in L-mode. The error bars represent the standard deviation of the velocity fit, averaged over the 1.2 msec. The variations in velocity are generally smaller in H-mode than in L-mode.

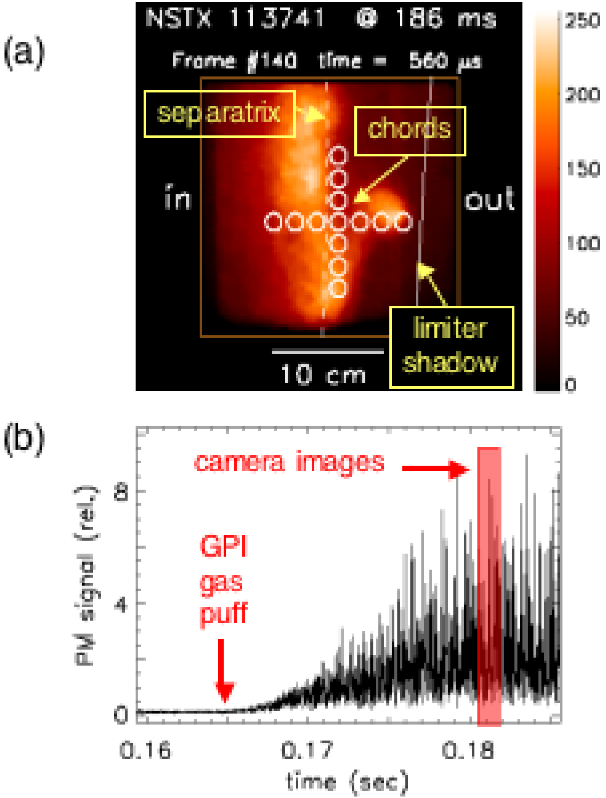(a)
NSTX 113741 @ 186 ms
Frame #140 time = 560 µs
separatrix
chords
in
out
limiter shadow
10 cm
250
200
150
100
50
0
(b)
camera images
GPI gas puff
PM signal (rel.)
0
4
8
0.16
0.17
0.18
time (sec)

Fig. 1

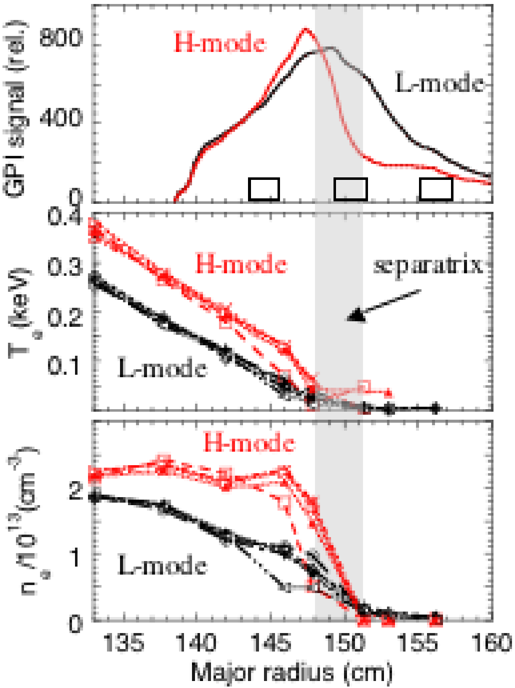
GPI signal (rel.)
800
400
0
H-mode
L-mode
0.4
0.3
0.2
0.1
T_e (keV)
H-mode
separatrix
L-mode
H-mode
L-mode
n_e /10^13 (cm^-3)
2
1
0
135
140
145
150
155
160
Major radius (cm)

Fig. 2

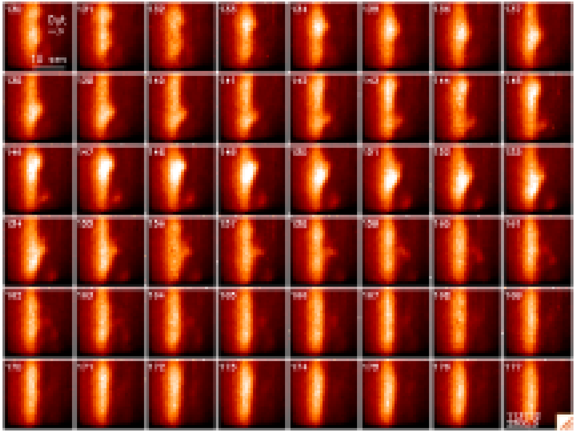

Fig. 3

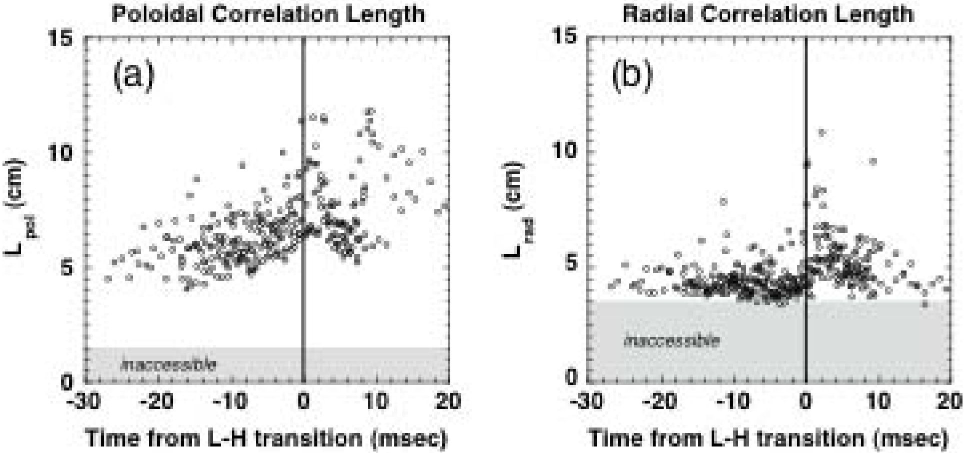
Poloidal Correlation Length
(a)
L_{pol} (cm)
15
10
5
0
inaccessible
-30
-20
-10
0
10
20
Time from L-H transition (msec)
Radial Correlation Length
(b)
L_{rad} (cm)
15
10
5
0
inaccessible
-30
-20
-10
0
10
20
Time from L-H transition (msec)

Fig. 4

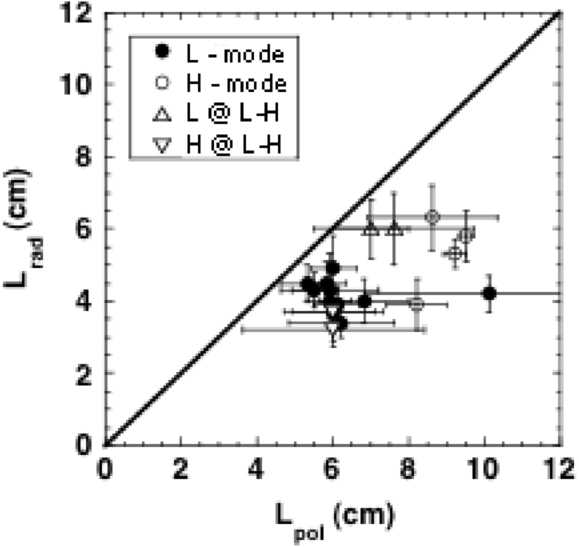

Fig. 5

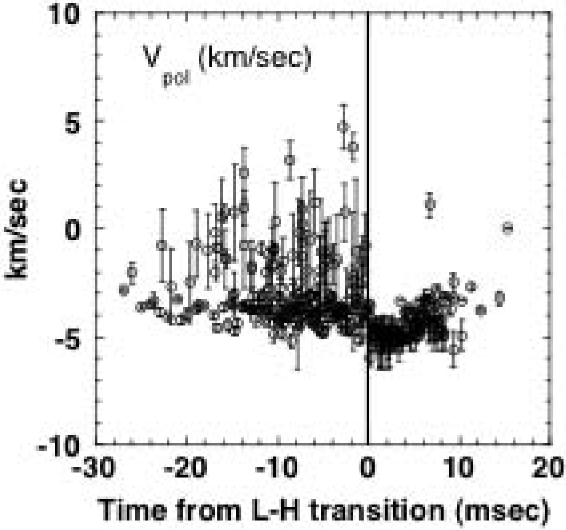

10
5
0
-5
-10
-30
-20
-10
0
10
20
V_{pol} (km/sec)
km/sec
Time from L-H transition (msec)

Fig. 6

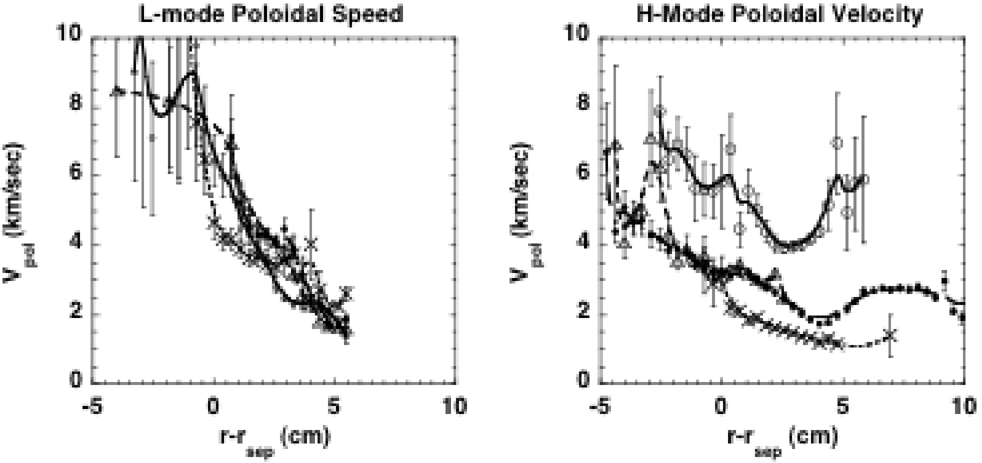
L-mode Poloidal Speed
H-Mode Poloidal Velocity
V_pol (km/sec)
r-r_sep (cm)
0
2
4
6
8
10
-5
0
5
10

Fig. 7